Fuel xxx (xxxx) 130770

Contents lists available at ScienceDirect

Fuel

journal homepage: www.elsevier.com/locate/fuel

Full Length Article

Promoting the valorization of blast furnace gas in the steel industry with the visual monitoring of combustion and artificial intelligence

P. Compais [a], J. Arroyo [a], F. Tovar [a], V. Cuervo-Piñera [b], A. Gil [c]

[a] CIRCE Technology Center, Parque Empresarial Dinamiza Avenida Ranillas, 3D 1ª Planta, 50018 Zaragoza, Spain

[b] ArcelorMittal, PO Box 90, Avilés 33480, Spain

[c] Universidad de Zaragoza, IUI mixto CIRCE, Campus Rio Ebro, Mariano Esquillor Gómez, 15, 50018 Zaragoza, Spain

ARTICLE INFO

Keywords:
Combustion monitoring
Predictive model
Color images
Industrial furnace
Steelmaking processes
Machine learning

ABSTRACT

The sustainability and decarbonization of processes in the steel industry are enhanced with the valorization of the gas generated during the chemical reactions produced in blast furnaces. However, the combustion of blast furnace gas (BFG) faces the drawback of lower flame stability, which increases the chance of operation shifts towards abnormal conditions and even the flashback or extinction of the flame. Thus, early detection and correction of regime deviations are needed to increase combustion efficiency, for which image-based systems have a high potential. This work focuses on monitoring an industrial furnace for steelmaking processes based on estimating O_2 concentration in flue gases using color images captured inside the combustion chamber. An experimental campaign was performed in a 1.2-MW burner to develop the supervision system, using three fuel blends of BFG and natural gas. Images were processed to extract intensity and textural features, which were used to train predictive models based on machine learning algorithms: logistic regression, support vector machines, and artificial neural networks (multilayer perceptron). O_2 concentration in flue gases was correctly estimated for at least 97 % of all the test samples and fuel blends. This study shows the potential of image-based systems for the automated control of BFG combustion at the industrial scale.

1. Introduction

Steel is crucial in modern societies as the third most manufactured bulk material, with 1.9 billion tons of world yearly production [1]. Steelmaking is also an energy-intensive industry, accounting for 8 % of global energy demand and 7 % of CO_2 direct emissions from the worldwide energy system. Reducing these quantities is urgent for the European Union, the second-largest steel producer. Consequently, Europe has ambitious targets for steel decarbonization, cutting emissions by 55 % by 2030 and reaching climate neutrality by 2050. Several strategies can help achieve these objectives, such as valorizing gaseous waste streams from the steel production processes. Blast furnaces, used in the basic oxygen steelmaking process to reduce iron ore, are a significant source of waste streams. Chemical reactions inside blast furnaces generate a by-product, the blast furnace gas (BFG), which can be used as fuel in other steelmaking furnaces, reducing natural gas (NG) consumption.

BFG differs from traditional fuels in its large concentration of inert gases and low calorific value. With a typical composition of 1–7 %vol. H_2, 18–25 %vol. CO_2, and 20–28 %vol. CO, balanced with N_2 [2], BFG has a lower heating value (LHV) around 3.3 MJ/Nm^3, one-tenth the calorific value of NG. Even though BFG reduces the thermal energy released during combustion, it can be used in high-temperature processes (such as steel reheating furnaces) by adopting multiple strategies. These solutions include its mixture with NG or coke oven gas (COG) [3], preheating of the combustion air [4], flameless combustion [5,6], and the use of several burner technologies (oxy-fuel, double regenerative and regenerative flat flame) [7].

The combustion of BFG and low-calorific fuels has been analyzed in the past by several numerical and experimental approaches. Regarding the steel industry, BFG and other by-product combustion gases were analyzed by Caillat [3] for their use in reheating furnaces and annealing lines. The study discussed the constraints due to the by-products' variable composition and physical properties. Cuervo-Piñera et al. [7] tested three burner technologies (oxy-fuel, double regenerative, and regenerative flat flame) for the combustion of BFG in steel reheating furnaces. The trials successfully proved the operation of these furnaces with only BFG, supplying oxygen or meeting other specific conditions. However, the economic viability of these alternatives should be checked for each facility, considering fuel saving, oxygen consumption, burner replacement, and retrofitting investment. The combustion of BFG/NG fuel blends was also simulated and validated for a semi-industrial furnace in the steel sector [8]. The authors analyzed velocity, temperature, OH and O_2 concentrations, and NO_x rate generation. The significant differences in the LHV of the fuel blend modified combustion fluid dynamics, affecting flow pattern, heat transfer, and temperature gradients in the furnace and, thus, process quality. Other works also analyzed the BFG combustion more broadly outside the steel industry. For instance, laminar flame characteristics were studied for several initial conditions and fuel compositions [2]. Moreover, composition, temperature, and fuel-switching effects were evaluated for the combustion stability of hot air heaters [4]. A critical ambient temperature was maintained to achieve stable combustion, which can be reduced by increasing the H_2 proportion in the blend from 1 to 5 %vol. Furthermore, mixtures of BFG and COG required a large concentration of BFG, higher than 80 %vol., to inhibit temperature oscillations.

Indeed, another consequence of the low LHV of BFG is the appearance of combustion instabilities [2,4]. Thus, disturbances under regular furnace operation may cause more severe deviations than other higher volumetric-energy density fuels. Early detection of these changes is essential to adjust the process quickly and reduce the period under suboptimal conditions, optimizing the overall operation. Thus, monitoring fuel blends with BFG is particularly interesting due to its lower combustion stability. In this aspect, image-based systems are a promising alternative to detect early deviations when burning fuels blended with BFG.

Image-based systems are essential in the state-of-the-art of combustion monitoring. This technology relies upon acquiring flame images and their correlation with combustion conditions. For example, images have been employed to estimate variables related to the air–fuel equivalence ratio, such as the air ratio [9], combustion regimes [10,11], and O_2 concentration in flue gases ($[O_2]_{fg}$) [12]. In contrast to conventional sensors, a single camera could simultaneously monitor several burners captured in the same pic-

https://doi.org/10.1016/j.fuel.2023.130770
Received 31 October 2023; Received in revised form 13 December 2023; Accepted 26 December 2023
0016-2361/

ture. To monitor the combustion, image-based systems perform several activities employing computer vision and machine learning (ML). Like other industrial problems, these tasks can be categorized into image acquisition, pre-processing, segmentation, feature extraction, and interpretation [13]. ML techniques lead the interpretation step, in which image features are transformed (modeled) into variables related to the combustion process. Nowadays, ML provides a set of horizontal techniques for data analysis and modeling. For example, in the field of combustion, ML has been used to predict operation parameters [14], exhaust gas temperature [15], emissions [16,17] and performance [16–18]. Unlike most literature research, the application of computer vision and ML techniques is limited for commercial camera systems installed in the industry. For example, market tools do not include the interpretation step, which depends on a human worker to analyze the information. Moreover, software suppliers generally do not include segmentation and feature extraction tools.

Image-based systems have also been used to monitor BFG combustion. Zheng et al. [2] employed a high-speed camera to compute the laminar burning velocity of BFG fuel blends. Earlier work by the authors [19–21] focused on image monitoring for steel industry applications. In this aspect, a preliminary study assessed the feasibility of combustion monitoring with a color camera in an industrial furnace [19]. At the laboratory scale, emission spectra, color, and radical images were captured and deeply analyzed for optical supervision of BFG combustion, showing strong dependencies with BFG concentration and equivalence ratio [20]. Furthermore, slight combustion variations were detected with accuracies from 0.78 to 0.97, processing flame images and training predictive models [21].

Nevertheless, monitoring BFG combustion at the industrial scale has not been studied in detail in the open literature. Therefore, image processing requires further analyses to tackle differences between lab and industrial levels. This work focuses on that research gap and proposes an image-based system to predict BFG combustion states to increase steelmaking process efficiency and address industry particularities. Trials are performed to analyze the new image processing with an experimental industrial furnace and a 1.2 MW burner used in steel production. A commercial vision system with a transfer device, cooling, and control unit acquired color images of flames, which are processed to predict $[O_2]_{fg}$ by ML algorithms. In addition, image processing is analyzed for the optimum fuel blend under controlled emissions and transient temperature states. The monitoring system is evaluated for three fuel blends under steady emissions and temperature conditions.

In this work, natural gas was used as a baseline, and two blends (70 and 80 BFG %vol.) were studied. These blends are extracted from the blast furnace line of the Asturias plant and are used by ArcelorMittal in their industrial processes to reduce natural gas consumption. The study will aid in promoting higher valorization of BFG and lower NG consumption in steelmaking industries. This contributes to reducing the pollutant emissions from fossil fuels, while a subproduct of the steel production process is valorized within the same plant where it is produced. From a global perspective, large amounts of process gas (BFG), which can be used as fuel in steel production processes, are available at steel production plants [22]. For the case of the ArcelorMittal Asturias plant, it has been estimated that the use of the whole amount of BFG in the steel production processes would involve a reduction of 52.8 kWh per ton of steel produced, with savings of 2.6 € per ton of steel and a decrease of 13.2 kg of CO_2 equivalent per ton of steel.

2. Material and methods

2.1. Experimental setup

The results presented in this work were obtained during a test campaign performed in an industrial testing furnace installed in the facilities of the ArcelorMittal Asturias plant in Spain (Fig. 1). The combustion chamber has the following dimensions: 4.6 m in length, 1.5 m in width, and 2.8 m in height. The furnace accepts different burners up to 1.2 MW of thermal input power and maximum working temperatures of around 1350 °C. These burners can be fueled with NG and with the off-process gases produced in the plant (COG and BFG). Using the same fuels as in the large plant ensures realistic results and avoids issues related to changes in gas composition at different scales. This way, the solution can be scaled up to other plant furnaces without this problem [8].

In the experimental trials, a diffusion burner is employed (Fig. 2). It allows the use of various gaseous fuel blends utilizing different fuel and air injection configurations. In particular, the burner has one central lance, two side lances for fuel, and multiple air inlets.

A water circuit with six semi-circular lances simulates the heat transferred from an industrial furnace to a steel strip. The water enters the circuit through the nearest lance to the burner and increases in temperature as it flows through the other conducts. At the end of the circuit, a fluid cooler reduces the water temperature before being reintroduced to the lances. The furnace has a control and data acquisition system for registering flow, temperatures, pressure, oxygen concentration in flue gases ($[O_2]_{fg}$), and pollutant emissions (CO, NO_x, SO_2, and CO_2). Five thermocouples measure combustion chamber temperature (T_{cc}) at different locations. The furnace can be configured to work with different gaseous blends and allows testing different configurations, such as preheated combustion air and O_2 injection.

Fuels with different compositions are tested in the experimental furnace. They are identified as 100 %vol. NG (BFG0), 30 %vol. NG and 70 %vol. BFG (BFG70), and 20 %vol. NG and 80 %vol. BFG (BFG80). BFG0 and BFG70 were also studied in a previous work [8]. BFG is extracted, filtered, and fed to the furnace directly from the plant's blast furnaces. Its composition is subjected to variability, influenced by the chemical processes inside the blast furnace [7]. A typical composition and LHV of the fuel blends are shown in Table 1.

The increase of BFG share in the fuel blend reduces NG consumption, leading to savings in fossil fuel consumption. However, higher concentrations of BFG raise difficulties in reaching the high temperatures needed during the steel production process. Additionally, the lower calorific value of BFG requires higher gas flow rates to meet the thermal energy demands, which could potentially result in operational issues in larger furnaces. Therefore, the use of BFG in the fuel blend is limited, and a certain NG share is required to ensure a stable operation. Considering this, BFG70 was defined as the optimum fuel blend. BFG80 was studied as an operative but suboptimal fuel, while BFG0 was analyzed as a baseline.

A commercial camera system was deployed inside the furnace through a viewing port in front of the burner. The devices included a BASLER BIP2-1920c color camera. The camera has a CMOS sensor, which provides a resolution of 2 MP at 30 frames per second. The camera is protected by a water-cooled metallic case installed on a SOBOTTA automatic transfer device which allows the introduction and extraction of the system inside the furnace. This device protects the optical system by retracting the camera from the furnace when detecting harmful temperatures or system malfunctions.

The image acquisition parameters of the camera were fixed during all the trials to obtain equivalent and comparable images. As a first step, the configuration of the exposure time was optimized by analyzing images and histograms under different conditions, avoiding under- or over-exposed images under any condition.

A data acquisition software recorded the images synchronously to measured variables (process information such as furnace temperatures, gas/air flow rates, pollutants or oxygen concentrations).

2.2. Methods

This section includes the methodology used in the research for furnace operation and flame processing.

2.2.1. Furnace operation

The furnace was pre-heated before the tests to reach steady conditions for emissions and temperature. Temperature was evaluated by averaging the measures of T_{cc} on five different points. Flue gas emissions stabilized thirty minutes after the start, but the tem-

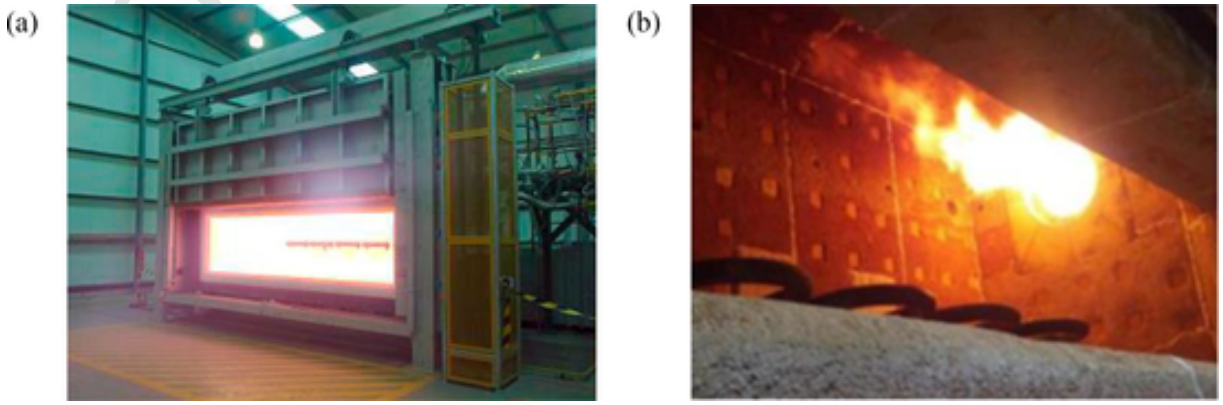

Fig. 1. The ArcelorMittal experimental furnace used for the tests [23].

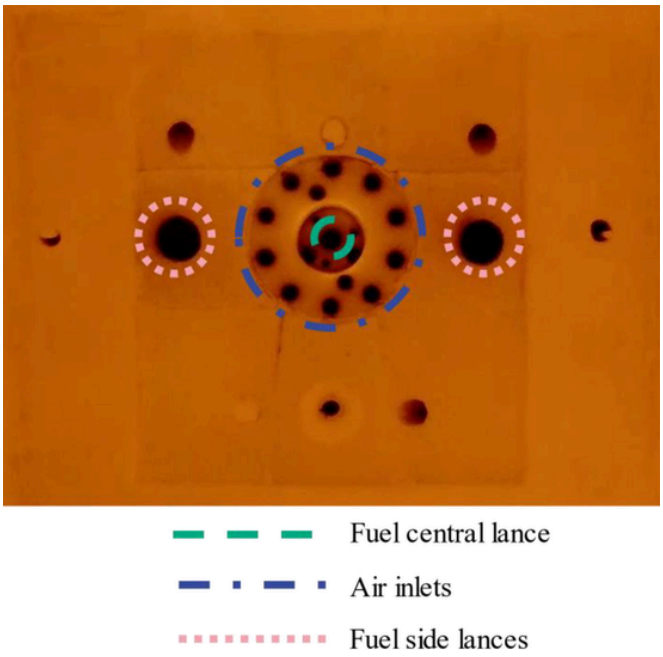

Fig. 2. View of the diffusion burner installed in the furnace.

Table 1
Fuel blends typical composition.

Fuel blend	BFG0	BFG70	BFG80
[CH_4] (%vol.)	92	28	18
[C_2H_6] (%vol.)	8	2	2
[N_2] (%vol.)	–	34	39
[CO] (%vol.)	–	16	18
[CO_2] (%vol.)	–	15	18
[H_2] (%vol.)	–	3	3
[H_2O] (%vol.)	–	1	1
[O_2] (%vol.)	–	1	1
LHV (MJ/Nm^3)	38	14	10

perature remained transient. When the heating reached 8 h, both emissions and temperature were constant. These two working conditions were labeled steady emissions and transient temperature (SETT) and steady emissions and steady temperature (SEST). The fuel flow rate (and, consequently, the calorific power rate introduced) was constant for each fuel blend. In contrast, the air-flow rate was slightly modified to reach different operation conditions. This resulted in different amounts of excess oxygen in flue gases ($[O_2]_{fg}$), depending on the blend composition and the combustion stoichiometry. Table 2 lists the tests' working conditions, fuel blends, combustion modes, and $[O_2]_{fg}$ concentrations in flue gases.

Table 2
Summary of the experimental tests.

Campaign	EXP1	EXP2	EXP3	EXP4
Working condition	SEST	SEST	SEST	SETT
Fuel blend	BFG0	BFG70	BFG80	BFG70
Combustion mode	Regular	Regular	Flameless	Regular
$[O_2]_{fg,1}$ (%vol.)	0	0	0	1
$[O_2]_{fg,2}$ (%vol.)	1	1	1	2
$[O_2]_{fg,3}$ (%vol.)	5	5	5	3
$[O_2]_{fg,4}$ (%vol.)	–	–	–	4
$[O_2]_{fg,5}$ (%vol.)	–	–	–	5

Each fuel blend under SEST conditions was tested for 0, 1, and 5 %vol. $[O_2]_{fg}$ (sub-stoichiometric, near-stoichiometric and over-stoichiometric conditions). Moreover, BFG70 was studied under SETT state for 1, 2, 3, 4, and 5 %vol. $[O_2]_{fg}$.

Fuel was injected through the central lance for all tests except for BFG80. Main and side burner lances were employed to improve the burner operation with that fuel blend, which implies different combustion modes. In this configuration, the reactants were strongly diluted with combustion products, and the burner operated in a flameless mode [5]. Flameless combustion is also known as moderate or intense low oxygen dilution (MILD), and it has a more significant reaction zone throughout the combustor volume. This distribution promotes a reduction in peak flame temperature and NO_x emissions [5,24]. The term "flameless" indicates that flames have a lower visibility than conventional flames, but the human eye may still detect them in some cases [24]. For instance, Reddy et al. [25] and Yetter et al. [26] recognized flames under flameless conditions.

Air was preheated at 485 ± 35 °C (21 %vol. O_2 concentration), fuel thermal power varied around 920 ± 15 kW, and T_{cc} around 1285 ± 75 °C. The tests for the three fuel blends provided the same thermal power by modifying the fuel flow rate three to four times higher for BFG70 and BFG80, respectively, compared to BFG0. A 10-minute video was captured during each test, and 1875 flame images were analyzed with an approximate frame rate of 3 images per second. For example, fourteen video fragments (one per test) of 1 s each are available as **supplementary material**. All the fragments are enclosed in a single video, which includes text in each frame to define the associated working condition, fuel blend, and $[O_2]_{fg}$.

2.2.2. Flame processing

Methods for processing flame images are partially based on the feature extraction and interpretation methodology detailed in previous work [21]. However, a significant modification is introduced to adapt the system to the industrial scale by removing the flame-segmentation step.

For the visual monitoring of combustion, flame segmentation is an alternative that can be applied before the feature extraction step. However, its use is not extended to all cases. Flame segmentation classifies image pixels into flame and non-flame groups, enabling the extraction of characteristics from only flame pixels. For instance, Mathew et al. [27] and Katzer et al. [28] employed thresholding to segment flames. Without flame segmentation, features are extracted from the whole image [9,12]. Other works based on deep learning did not perform an explicit flame segmentation, although it could be implicitly included to some extent in the layer operations [10,11]. Bai et al. [9] remarked on the complexity of defining flame boundaries, which can be inaccurate and lead to low performance in monitoring. Identifying the flame body could be easier for flames with more stability and simpler geometry. This is the case of previous authors' work [20], in which flames had a simpler and similar geometry for different combustion conditions. However, image flames processed by Bai et al. [9], Abdurakipov et al. [10], Han et al. [11], and Yang et al. [12] were more diffuse and variable. Therefore, their segmentation could be more complex. Furthermore, the difficulty of flame segmentation also depends on the image background and the appearance of other non-flame elements. For instance, in the studies of Bai et al. [9], Abdurakipov et al. [10], and Han et al. [11], the background was empty, and thus, the classification of pixels into flame and non-flame groups could be more straightforward. Nevertheless, in [19], flames appeared over the furnace background.

To sum up, the complexity of flame segmentation depends on the use case considered in each study. The present research focuses on the same industrial furnace and similar flue blends from the work of Compais et al. [19]. Therefore, segmentation would have the challenge of identifying flames from the furnace background. Moreover, a preliminary inspection of the furnace operation ensured the diffuse and variable geometry of the flames, which would increase the segmentation complexity even more. Thus, due to the high risk of inaccurately identifying flames and lowering the monitoring performance, the present research modifies the procedure of Compais et al. [21] by removing the flame-segmentation step. This more straightforward method could be more suitable for future implementation of the monitoring system at the industrial level, in which unseen flame images and combustion conditions may appear over time.

The flame processing used in this research is summarized in Fig. 3. It consists of extracting 51 features and their interpretation to predict $[O_2]_{fg}$. Flame segmentation is not applied, and image variables are computed from the whole image.

Regarding the feature extraction step, a wide range of image characteristics can be considered for combustion analysis. Standard features are based either on intensity [9,27–29], geometry [28], or texture measures [9,12]. Intensity and texture characteristics

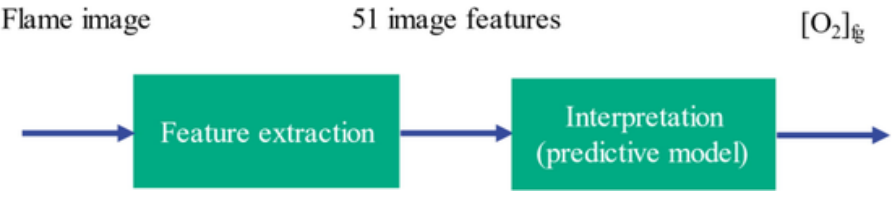

Fig. 3. Method for the processing of flame images.

can be extracted from the entire image or specific flame pixels. Geometry features generally calculate properties of the flame body, such as length and area [28], and therefore, they require the application of flame segmentation. Usually, each study manually selects a limited group of features tailored to its use case. This work computes a subset of the characteristics from the work of Compais et al. [21], including only those of intensity and textural type. Geometrical features are not analyzed because the present work does not apply flame segmentation. The feature subset comprises 51 variables per color image, and the extraction method is shown in Fig. 4.

The three-color channels of the image (red, green, and blue) are considered separately, analyzing their corresponding monochrome images. Each color channel is processed to extract four intensity features (mean, standard deviation, skewness, and kurtosis of the pixel intensities [21,29]) and compute its gray level co-occurrence matrix (GLCM). This matrix is employed to define thirteen textural features selected from the work of Haralick et al. [30] and also used in other studies [9,21].

Predictive models estimate combustion conditions based on image properties in the final interpretation processing step. With that purpose, the present work uses the same ML method described in [21] to train and test models based on the experimental campaign performed at an industrial scale. The procedure comprises analysis of variance (ANOVA) *F*-tests for feature selection and nested cross-validation (CV) for hyperparameter tuning and performance evaluation. The same ML algorithms analyzed in [21] are tested at an industrial scale in the current work.

Three ML algorithms are studied: logistic regression (LR) [10,11], support vector machines (SVM) [9–11], and artificial neural networks (ANN) [9–11]. A multilayer perceptron (MLP) is defined for the latter with a single hidden layer of 100 neurons. Flame images are labeled according to their associated $[O_2]_{fg}$, and the models classify them into three or five discrete $[O_2]_{fg}$ values. The whole set of images of each experimental campaign is split into training and test sets. The training set is used to automatically select a subset of image characteristics as input, tune hyperparameters, and evaluate the performance of the ML algorithms. Finally, the best algorithm is assessed again, employing the test set. The input subsets of image features include the ten variables with the highest variance for the $[O_2]_{fg}$ classes. These characteristics are selected using ANOVA *F*-tests. The hyperparameter tuning and performance evaluation of the training set are implemented in a nested CV procedure. An outer CV of ten folds splits the training set into ten pairs of training and validation subsets. The accuracy of each training and validation subset is computed and averaged for each ML algorithm. For each training subset, model hyperparameters are selected with an inner CV of five folds. The training subset is split into five pairs of training and validation subsets, for which several combinations of hyperparameters were evaluated with the model's accuracy. After the nested CV, the ML algorithm with the best performance is analyzed in more detail by computing its confusion matrixes for the validation subsets of the four experimental campaigns. Next, the chosen ML algorithm is re-evaluated with the test set, measuring its test accuracy and comparing it with the achieved for training and validation.

Python is used as a programming language (version 3.7) to develop the code for image processing and predictive models. The following libraries are also employed: OpenCV, Scikit-learn, NumPy, SciPy, Mahotas, and Pandas.

3. Results and discussion

3.1. Flame images for the working conditions, fuel blends, and $[O_2]_{fg}$

Fig. 5 shows flame images captured for SEST conditions and the fuel blends of BFG0, BFG70, and BFG80 at different $[O_2]_{fg}$. In the case of BFG70, images captured for SETT were also studied (Fig. 6). For each working condition (SEST or SETT), fuel blend and $[O_2]_{fg}$, Fig. 5 and Fig. 6 include a single image, which corresponds to the first frame captured in its associated test. Therefore, the images shown were captured at least 8 h or 30 min apart from each other, which are the required time intervals to achieve SEST or SETT conditions, respectively.

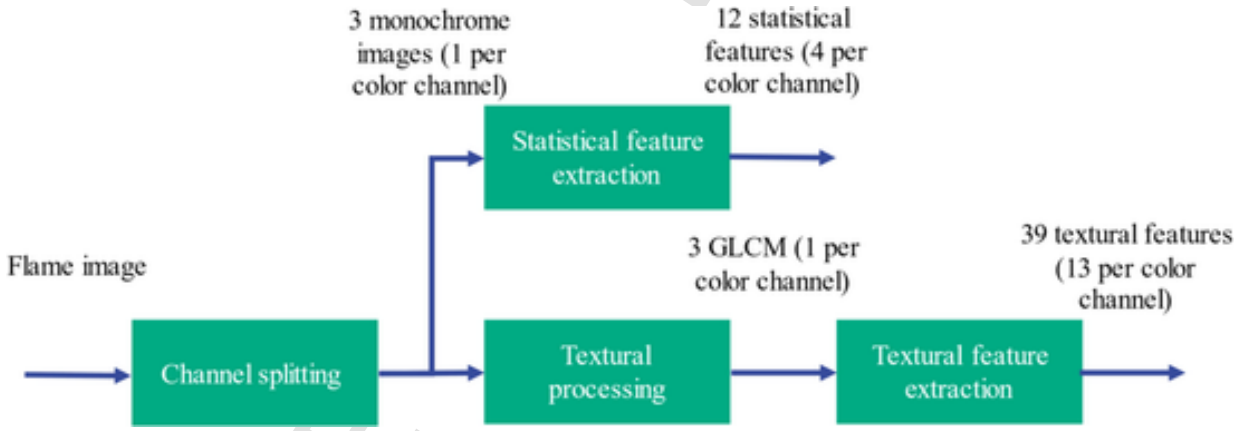

Fig. 4. Method for feature extraction of flame images.

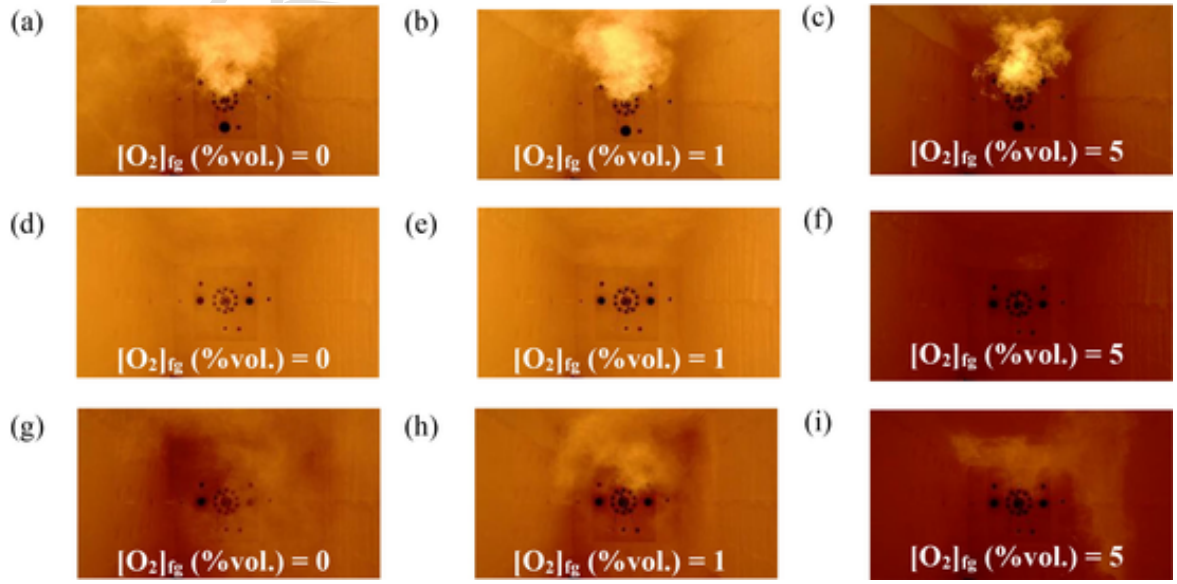

Fig. 5. Flame images for SEST and (a) BFG0, (b) BFG70, and (c) BFG80.

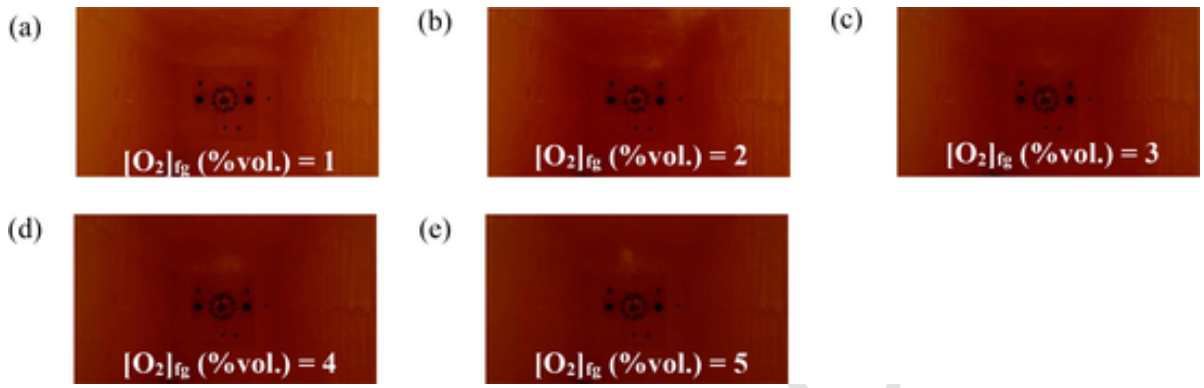

Fig. 6. Flame images for SETT and BFG70 with $[O_2]_{fg}$ of (a) 1, (b) 2, (c) 3, (d) 4, and (e) 5 %vol.

The red color channel predominates over blue and green in diffusion flame images. While premixed flames are bluish and dominated by chemiluminescence, diffusion flames are orangish and characterized by their soot emission [31]. Soot particles emit blackbody radiation [32], ideally described by Planck's law [33]. According to this law, an object at a higher temperature emits higher radiation. Indeed, soot temperature and volume fraction can be retrieved from flame images [34]. The longer period of furnace preheating under SEST conditions caused higher T_{cc} (Fig. 7) and generated brighter images (Fig. 5.e and Fig. 5.f) than SETT ones (Fig. 6.a and Fig. 6.e). In contrast to premixed flames, the color of diffusion flames has a lower dependence on the reactant composition and equivalence ratio [35]. Still, this work detected differences under SEST conditions.

Flames had significantly lower visibility for the fuel blend of BFG70 and BFG80 concerning BFG0. In particular, BFG70 flames in static images were hardly visible to the human eye. In contrast, its capture on video helped their recognition due to the detection of variations in the flame geometry and location in the furnace. The lower visibility of flames for BFG70 and BFG80 is caused by the large volume fraction of inert gases in the fuel, with around 35 %vol. and 15 %vol. of N_2 and CO_2 concentrations, respectively. A similar behavior was detected in [32], where the OH* chemiluminescence peak was reduced when the N_2 dilution for CH_4 diffusion flames was increased. BFG80 images (Fig. 5.g, Fig. 5.h, and Fig. 5.i) also captured the widespread distribution of flames, which is characteristic of flameless combustion.

$[O_2]_{fg}$ was related to T_{cc} as shown in Fig. 7. In this work, $[O_2]_{fg}$ of 1 %vol. corresponds to near-stoichiometric conditions (where air and fuel flow rates were fixed to produce stoichiometric combustion). Therefore, concentrations below or above that value are related to sub-stoichiometric or over-stoichiometric conditions, respectively. Considering this, temperature trends in Fig. 7 follow the expected behavior of adiabatic flame temperature concerning air–fuel equivalence ratio, reaching maximum temperature for near-stoichiometric conditions.

The brightness of the image increased when the operation moved toward stoichiometric conditions. Both significant and slight image changes were reported based on the temperature variations. For SEST conditions and the same fuel blend, images differed significantly between 1 and 5 %vol $[O_2]_{fg}$. This behavior was slighter for SETT conditions, which reached lower T_{cc} than the SEST regime. Furthermore, in all the tests, images were similar for variations of $[O_2]_{fg}$ around 1 %vol.

3.2. Selection of image characteristics for the estimation of $[O_2]_{fg}$

As described in the methods for flame processing, the initial set of 51 features was manually selected based on the state of the art. To summarize, previous works have monitored combustion with intensity [21,29] and texture features [9,21] considered in this work. The image properties used in this work have been validated for the flame characterization of similar fuel blends at lab scale [21].

From the total of 51 image properties, a subset of ten features was selected using ANOVA *F*-tests. This analysis measured the variance of image features with $[O_2]_{fg}$. Critical *F*-values were computed for each experimental campaign with a 0.05 confidence level, resulting in 3.00 (SEST) and 2.37 (SETT). The critical *F*-value was the same for the tests with SEST conditions because they included the same population (classes of O_2 concentration in flue gases) and number of samples (flame images per experimental campaign). All the *F*-values of image features were at least an order of magnitude higher than the critical *F*-value of their experimental campaign. Therefore, the classes of $[O_2]_{fg}$ affected the mean values of every extracted image feature for regular and flameless combustion. This result proves that the application of flame segmentation was not necessary for these use cases since characteristics from the whole image are effective descriptors of the $[O_2]_{fg}$.

The subset of ten image features with higher *F*-values was used for each experimental campaign to feed predictive models. All the subsets comprise characteristics from the two types of features (intensity and textural) and three-color channels (red, green, and blue), except for SETT. For the latter tests, properties were not computed from the blue channel. In particular, the mean intensity of the pixel values for the red channel had a significant role in all the subsets (Fig. 8). The general behavior of this image feature matched the brightness and temperature changes previously discussed (Fig. 5, Fig. 6 and Fig. 7).

3.3. Evaluation of predictive models for the estimation of $[O_2]_{fg}$

Predictive models were adjusted to estimate $[O_2]_{fg}$ based on the subsets of ten image features. Three different ML algorithms (LR, SVM, and MLP) were studied for each fuel

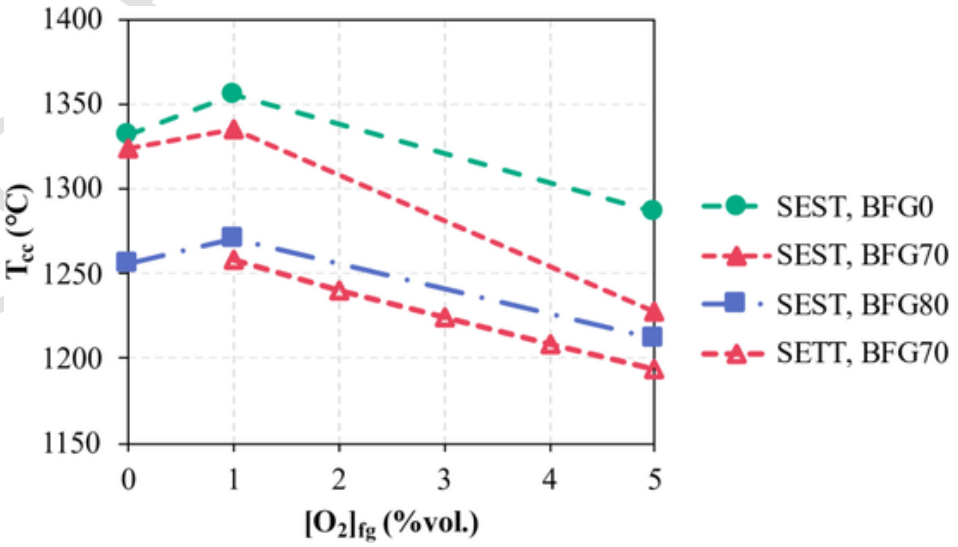

Fig. 7. T_{cc} during the experimental tests.

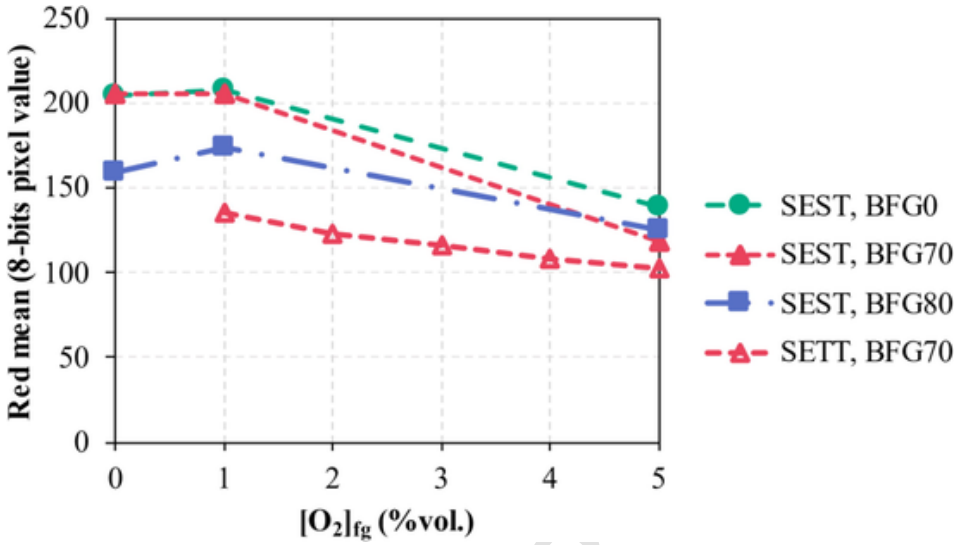

Fig. 8. Image feature of red mean versus $[O_2]_{fg}$. (For interpretation of the references to color in this figure legend, the reader is referred to the web version of this article.)

blend. A nested CV was employed to train and validate the predictive models and tune hyperparameters, achieving significant accuracies (Table 3).

Predictive models reached validation accuracies around 0.995, which were lowered to 0.960 for the fuel blend of BFG70 and SEST conditions. Similar results were obtained for the three ML algorithms. However, SVM provided the highest accuracy in all the cases, outperforming ANN, as in [21] and [36]. The higher performance of a specific algorithm could be promoted by its particular characteristics. While LR fits a probability model based on logistic functions, SVM adjusts a hyperplane between classes, maximizing the margin between them. By contrast, MLP is a feed-forward artificial neural network, whose neurons are trained by back-propagation. However, the reduced difference in accuracy between the algorithms (below 1 %) limits the extrapolation of SVM as the best choice. Generalizability, and interpretability (black-box nature) are advanced research lines for ML techniques applied to combustion [37].

Table 3
Validation accuracies of the predictive models for estimating $[O_2]_{fg}$.

Campaign	EXP1	EXP2	EXP3	EXP4
Working condition	SEST	SEST	SEST	SETT
Fuel blend	BFG0	BFG70	BFG80	BFG70
LR (accuracy)	0.9920	0.9666	0.9970	0.9998
SVM (accuracy)	0.9936	0.9671	0.9980	0.9999
MLP (accuracy)	0.9866	0.9640	0.9962	0.9998

Fig. 9 shows the confusion matrixes of the predictive models based on that algorithm, for the validation subsets of all the experimental campaigns. According to the confusion matrixes, the predictive models achieved a balanced behavior, reaching high accuracies (0.9489 as a minimum) for all the $[O_2]_{fg}$ classes, fuel blends, and working conditions.

As a final evaluation, predictive models were adjusted employing the whole training set and the SVM algorithm. Hyperparameters were defined according to the best results of the nested CV, which were a linear kernel, a regularization term of 10 for the three experimental campaigns for SEST, and a regularization term of 0.1 for the tests of SETT. Finally, the accuracy of the models was measured for the test set. The training, validation, and test accuracy of the predictive models based on SVM are compared in Fig. 10.

The accuracy of the predictive models had a similar behavior for training, validation, and test sets without a significant influence of overfitting or underfitting. The predictive models achieved a high accuracy in estimating $[O_2]_{fg}$ based on flame images, although images may have slight variations that the human eye cannot perceive between different conditions. Furthermore, predictions were accurate even for low-visibility flames during regular or flameless combustion and transient conditions. Thus, automa-

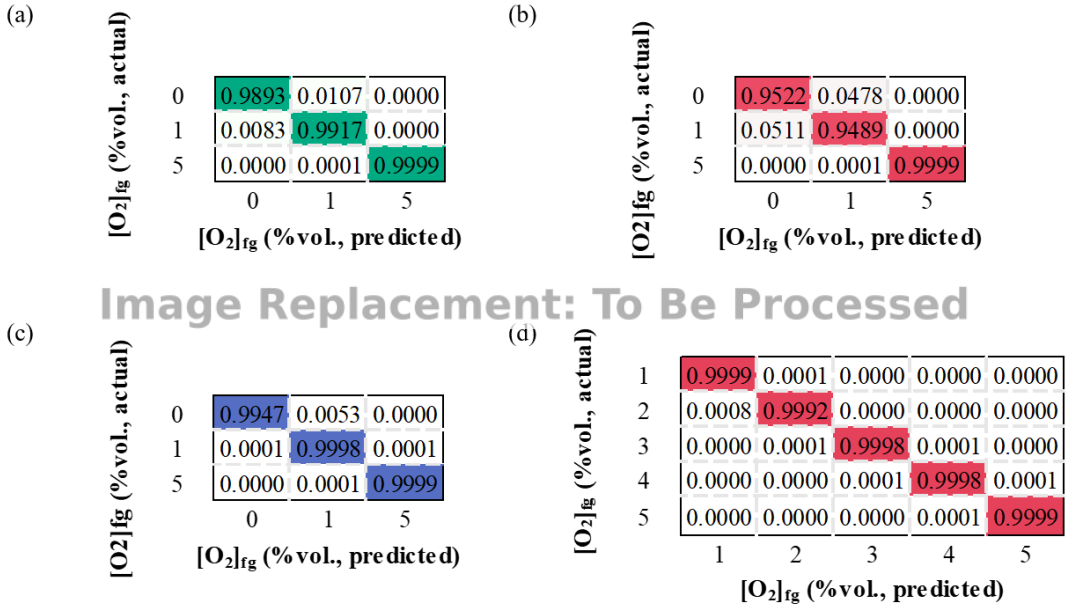

Fig. 9. Confusion matrixes of the predictive models based on SVM for the validation subsets of (a) SEST BFG0, (b) SEST BFG70, (c) SEST BFG80 and (d) SETT BFG70.

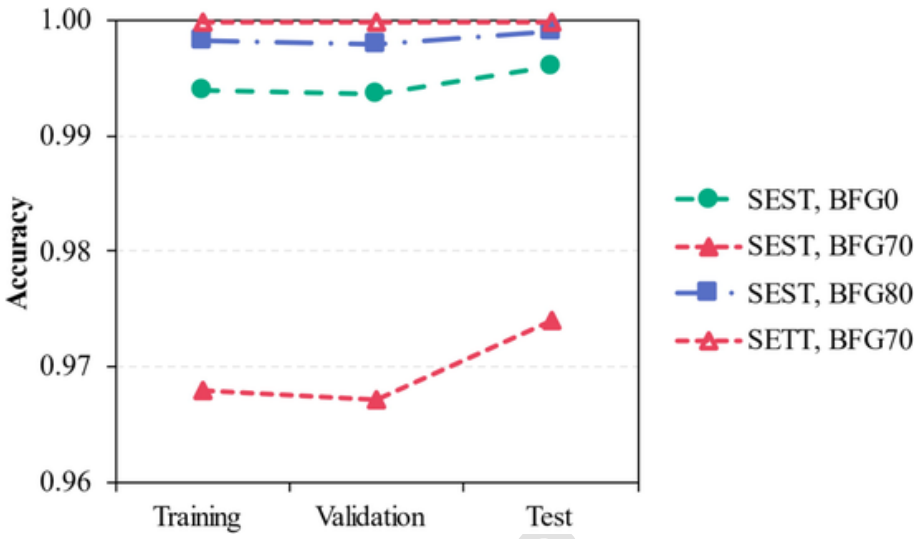

Fig. 10. Training, validation, and test accuracies of the predictive models based on SVM.

tion methods can enhance the visual monitoring of the combustion supervised by humans.

4. Conclusions

In this study, the combustion monitoring in the steel sector was analyzed by acquiring color images from the flames of an experimental industrial furnace with a diffusion burner. Predictive models were adjusted to estimate the $[O_2]_{fg}$ based on intensity and textural characteristics extracted from the images. This monitoring was developed for tests with a fixed thermal power of 925 kW, two stability conditions (steady and transient temperature), and three fuel blends (BFG0, BFG70, and BFG80) obtained by mixing NG with BFG. Predictive models were fed by subsets of the computed image features, defined by ANOVA *F*-tests, and comprised the characteristics of a higher variance with $[O_2]_{fg}$. Three ML algorithms (LR, SVM, and ANN-MLP) were studied for the predictive models. The accuracy of the algorithms was evaluated by employing training-test split and nested CV.

The main conclusions of this research are as follows.

- Color images were affected by the combustion conditions analyzed. Image brightness increased for higher T_{cc}, related to lower BFG share in the fuel and $[O_2]_{fg}$ closer to 1 %vol. Moreover, adding BFG to NG reduced flame visibility.
- Intensity and textural characteristics from the three-color channels of the images were highlighted as descriptors of $[O_2]_{fg}$ without requiring the application of flame segmentation.
- Predictive models fed by the image characteristics reached high accuracies during training, validation, and testing, with adequate behavior without overfitting or underfitting and a minimum value of 0.96. The use of different ML algorithms (LR, SVM, or ANN) did not significantly affect the results, which were slightly better for SVM.
- Predictive models accurately estimated variations in $[O_2]_{fg}$ during regular and flameless combustion, even when images had minor variations between them. This way, the visual monitoring of combustion performed by humans can be improved.

The current research sets the stage for automated flame monitoring at an industrial scale. The detection of changes in the combustion conditions allows for the correction of deviated parameters, helping to optimize the processes and avoid the appearance of critical instabilities. The results obtained in this study demonstrate high precision for the case analyzed in an industrial test facility incorporating an industrial burner commonly used in steel manufacturing processes. This facility's process conditions and image quality were optimal for model training and development. However, using raw material inside the furnace instead of simulated load could affect the accuracy of the models. The irradiance from the steel load could interfere with the image or create fumes or particles inside the furnace, which may require additional preprocessing.

Further developments should focus on applying the models to industrial furnaces, such as reheating or annealing furnaces, where multiple burners can be captured in a single image. Overall air and fuel flow rates are typically measured in these furnaces, making it challenging to detect imbalances if there are several burners. Applying the models developed in this work to the different burners could provide a valuable monitoring tool, potentially reducing maintenance costs when residual streams are used as fuel. For this application, other challenging aspects of image processing are expected, like the separate segmentation of each burner or interferences of the combustion of the different burners in the same field of view. Nevertheless, industrial furnaces offer interesting possibilities for camera installation and image acquisition, as external viewing ports, which can reduce investment costs, or the installation in optimal locations to monitor the areas of interest.

CRediT authorship contribution statement

P. Compais: Writing – review & editing, Writing – original draft, Validation, Software, Methodology, Investigation, Data curation, Conceptualization. **J. Arroyo:** Writing – review & editing, Writing – original draft, Supervision, Resources, Project administration, Methodology, Investigation, Conceptualization. **F. Tovar:** Writing – review & editing, Investigation, Formal analysis, Data curation. **V. Cuervo-Piñera:** Writing – review & editing, Validation, Supervision, Methodology, Investigation, Conceptualization. **A. Gil:** Writing – review & editing, Writing – original draft, Supervision, Methodology.

Declaration of competing interest

The authors declare that they have no known competing financial interests or personal relationships that could have appeared to influence the work reported in this paper.

Data availability

The data that has been used is confidential.

Acknowledgments

This work has been supported by the European Union's Horizon 2020 Research and Innovation Programme under Grant Agreement No. 820771 (BAMBOO project).

Appendix A. Supplementary data

Supplementary data to this article can be found online at https://doi.org/10.1016/j.fuel.2023.130770.

References

[1] IEA. Iron and steel technology roadmap. https://www.iea.org/reports/iron-and-steel-technology-roadmap; 2020 [accessed 11 September 2023].
[2] Zheng W, Pang L, Liu Y, Xie F, Zeng W. Effects of initial condition and fuel composition on laminar burning velocities of blast furnace gas with low heat value. Fuel 2021;289:119775. https://doi.org/10.1016/j.fuel.2020.119775.
[3] Caillat S. Burners in the steel industry: Utilization of by-product combustion gases in reheating furnaces and annealing lines. Energy Procedia 2017;120:20–7. https://doi.org/10.1016/j.egypro.2017.07.152.
[4] Zhang L, Xie W, Ren Z. Combustion stability analysis for non-standard low-calorific gases: blast furnace gas and coke oven gas. Fuel 2020;278:118216. https://doi.org/10.1016/j.fuel.2020.118216.
[5] Nguyen P.D, Ghazal G, Piñera V.C, Battaglia V, Rensgard A, Ekman T, et al. Modelling of flameless oxy-fuel combustion with emphasis on radiative heat transfer for low calorific value blast furnace gas. Energy Procedia 2017;120:492–9. https://doi.org/10.1016/j.egypro.2017.07.177.
[6] Nguyen H.T, Barnaud C, Domingo P, Nguyen P.D, Vervisch L. Large-eddy simulation of flameless combustion with neural-network driven chemistry. Appl Energy Combust Sci 2023;14:100126. https://

doi.org/10.1016/j.jaecs.2023.100126.
[7] Cuervo-Piñera V, Cifrián-Riesgo D, Nguyen P.D, Battaglia V, Fantuzzi M, Della Rocca A, et al. Blast furnace gas based combustion systems in steel reheating furnaces. Energy Procedia 2017;120:357–64. https://doi.org/10.1016/j.egypro.2017.07.215.
[8] Arroyo J, Pérez L, Cuervo-Piñera V. CFD modeling and validation of blast furnace gas/natural gas mixture combustion in an experimental industrial furnace. Processes 2023;11(2):332. https://doi.org/10.3390/pr11020332.
[9] Bai X, Lu G, Hossain M.M, Szuhánski J, Daood S.S, Nimmo W, et al. Multi-mode combustion process monitoring on a pulverised fuel combustion test facility based on flame imaging and random weight network techniques. Fuel 2017;202:656–64. https://doi.org/10.1016/j.fuel.2017.03.091.
[10] Abdurakipov S.S, Gobyzov O.A, Tokarev M.P, Dulin V.M. Combustion regime monitoring by flame imaging and machine learning. Optoelectron Instrum Data Process 2018;54:513–9. https://doi.org/10.3103/S875669901805014X.
[11] Han Z, Li J, Zhang B, Hossain M.M, Xu C. Prediction of combustion state through a semi-supervised learning model and flame imaging. Fuel 2021;289:119745. https://doi.org/10.1016/j.fuel.2020.119745.
[12] Yang G, He Y, Li X, Liu H, Lan T. Gabor-GLCM-based texture feature extraction using flame image to predict the O_2 content and NO_x. ACS Omega 2022;7:3889–99. https://doi.org/10.1021/acsomega.1c03397.
[13] Smith M.L, Smith L.N, Hansen M.F. The quiet revolution in machine vision - a state-of-the-art survey paper, including historical review, perspectives, and future directions. Comput Ind 2021;130:103472. https://doi.org/10.1016/j.compind.2021.103472.
[14] Liu J, Ulishney C, Dumitrescu C.E. Random forest machine learning model for predicting combustion feedback information of a natural gas spark ignition engine. J Energy Resour Technol 2021;143(1):012301. https://doi.org/10.1115/1.4047761.
[15] Liu J, Ulishney C, Dumitrescu C.E. Machine learning assisted prediction of exhaust gas temperature of a heavy-duty natural gas spark ignition engine. Appl Energy 2021;300:117413. https://doi.org/10.1016/j.apenergy.2021.117413.
[16] Huang Q, Liu J, Ulishney C, Dumitrescu C.E. On the use of artificial neural networks to model the performance and emissions of a heavy-duty natural gas spark ignition engine. Int J Engine Res 2022;23(11):1879–98. https://doi.org/10.1177/14680874211034409.
[17] Liu J, Huang Q, Ulishney C, Dumitrescu C.E. Comparison of random forest and neural network in modeling the performance and emissions of a natural gas spark ignition engine. J Energy Resour Technol 2022;144(3):032310. https://doi.org/10.1115/1.4053301.
[18] Liu J, et al. A support-vector machine model to predict the dynamic performance of a heavy-duty natural gas spark ignition engine. SAE Technical Paper 2021;2021-01-0529. doi:10.4271/2021-01-0529.
[19] Compais P Arroyo J González-Espinosa A Gonzalo-Tirado C Castán-Lascorz MA Barrio J et al. Experimental analysis of blast furnace gas co-firing in a semi-industrial furnace using colour images Proceedings of the 7th World Congress on Momentum, Heat and Mass Transfer 2022 117 /10.11159/csp22.117 .
[20] Compais P, Arroyo J, González-Espinosa A, Castán-Lascorz M.Á, Gil A. Optical analysis of blast furnace gas combustion in a laboratory premixed burner. ACS Omega 2022;7:24498–510. https://doi.org/10.1021/acsomega.2c02103.
[21] Compais P, Arroyo J, Castán-Lascorz M.Á, Barrio J, Gil A. Detection of slight variations in combustion conditions with machine learning and computer vision. Eng Appl Artif Intell 2023;126(Pt A):106772. https://doi.org/10.1016/j.engappai.2023.106772.
[22] Uribe-Soto W, Portha J.F, Commenge J.M, Falk L. A review of thermochemical processes and technologies to use steelworks off-gases. Renew Sustain Energy Rev 2017;74:809–23. https://doi.org/10.1016/j.rser.2017.03.008.
[23] European Commission, Directorate-General for Research and Innovation, Battaglia V, Niska J, Cuervo Piñera V, Fantuzzi M. High efficiency low NOX BFG based combustion systems in steel reheating furnaces (HELNOx-BFG): final report. Publications Office 2018. https://doi.org/10.2777/165777.
[24] Khidr K.I, Eldrainy Y.A, EL-Kassaby M.M. Towards lower gas turbine emissions: Flameless distributed combustion. Renew Sust Energ Rev 2017;67:1237–66. https://doi.org/10.1016/j.rser.2016.09.032.
[25] Reddy V.M, Sawant D, Trivedi D, Kumar S. Studies on a liquid fuel based two stage flameless combustor. Proc Combust Inst 2013;34(2):3319–26. https://doi.org/10.1016/j.proci.2012.06.028.
[26] Yetter R.A, Glassman I, Gabler H.C. Asymmetric whirl combustion: a new low NOx approach. Proc Combust Inst 2000;28(1):1265–72. https://doi.org/10.1016/s0082-0784(00)80339-2.
[27] Mathew A.P, Asokan A, Batri K, Sivakumar D. Comparative analysis of flame image features for combustion analysis. Indian J Sci Technol 2016;9:1–11. doi:10.17485/ijst/2016/v9i6/79904.
[28] Katzer C, Babul K, Klatt M, Krautz H.J. Quantitative and qualitative relationship between swirl burner operating conditions and pulverized coal flame length. Fuel Process Technol 2017;156:138–55. https://doi.org/10.1016/j.fuproc.2016.10.013.
[29] González-Cencerrado A, Peña B, Gil A. Experimental analysis of biomass co-firing flames in a pulverized fuel swirl burner using a CCD based visualization system. Fuel Process Technol 2015;130:299–310. https://doi.org/10.1016/j.fuproc.2014.10.041.
[30] Haralick R.M, Shanmugam K, Dinstein I. Textural features for image classification. IEEE Trans Syst Man Cybern 1973;SMC-3:610–21. https://doi.org/10.1109/TSMC.1973.4309314.
[31] Huang H.W, Zhang Y. Flame colour characterization in the visible and infrared spectrum using a digital camera and image processing. Meas Sci Technol 2008;19:085406. https://doi.org/10.1088/0957-0233/19/8/085406.
[32] He L, Guo Q, Gong Y, Wang F, Yu G. Investigation of OH* chemiluminescence and heat release in laminar methane–oxygen co-flow diffusion flames. Combust Flame 2019;201:12–22. https://doi.org/10.1016/j.combustflame.2018.12.009.
[33] Karnani S, Dunn-Rankin D. Visualizing CH* chemiluminescence in sooting flames. Combust Flame 2013;160:2275–8. https://doi.org/10.1016/j.combustflame.2013.05.002.
[34] Li T, Zhang C, Liu D. Simultaneously retrieving of soot temperature and volume fraction in participating media and laminar diffusion flame using multi-spectral light field imaging. Int J Therm Sci 2023;193:108472. https://doi.org/10.1016/j.ijthermalsci.2023.108472.
[35] Huang H.W, Zhang Y. Digital colour image processing based measurement of premixed CH4 + air and C2H4 + air flame chemiluminescence. Fuel 2011;90:48–53. https://doi.org/10.1016/j.fuel.2010.07.050.
[36] Han Z, Hossain M.M, Wang Y, Li J, Xu C. Combustion stability monitoring through flame imaging and stacked sparse autoencoder based deep neural network. Appl Energy 2020;259:114159. https://doi.org/10.1016/j.apenergy.2019.114159.
[37] Zhou L, Song Y, Ji W, Wei H. Machine learning for combustion. Energy AI 2022;7:1011128. https://doi.org/10.1016/j.egyai.2021.100128.